University of Rhode Island
DigitalCommons@URI

Open Access Master's Theses

2017

Dynamic Response of TI_2ALC Under Radial Confinement at High Temperature

Daniel Clarkin
University of Rhode Island, dsclarkin@my.uri.edu

Follow this and additional works at: https://digitalcommons.uri.edu/theses

Terms of Use
All rights reserved under copyright.

Recommended Citation
Clarkin, Daniel, "Dynamic Response of TI_2ALC Under Radial Confinement at High Temperature" (2017). *Open Access Master's Theses.* Paper 1062.
https://digitalcommons.uri.edu/theses/1062

This Thesis is brought to you by the University of Rhode Island. It has been accepted for inclusion in Open Access Master's Theses by an authorized administrator of DigitalCommons@URI. For more information, please contact digitalcommons-group@uri.edu. For permission to reuse copyrighted content, contact the author directly.

DYNAMIC RESPONSE OF TI_2ALC UNDER RADIAL CONFINEMENT AT HIGH TEMPERATURE

BY

DANIEL CLARKIN

A THESIS SUBMITTED IN PARTIAL FULFILLMENT OF THE

REQUIREMENTS FOR THE DEGREE OF

MASTER OF SCIENCE

IN

MECHANICAL ENGINEERING AND APPLIED MECHANICS

UNIVERSITY OF RHODE ISLAND

2017

MASTER OF SCIENCE THESIS

OF

DANIEL CLARKIN

APPROVED:

Thesis Committee:

Major Professor Arun Shukla

Hongyan Yuan

Richard Vaccaro

Nasser H. Zawia
DEAN OF THE GRADUATE SCHOOL

UNIVERSITY OF RHODE ISLAND
2017

ABSTRACT

Experiments were performed to evaluate the dynamic mechanical response of MAX phase material Ti2AlC at high temperature (HT) and under radial confinement. A Split Hopkinson Pressure Bar (SHPB) apparatus was employed to conduct experiments at a strain rate of 500 s 1. High speed photography was used to capture the dynamic response of unconfined specimens. An induction coil was used to heat the specimens from 25 to 1000°C. Nickel-cobalt-ferrous alloy (Kovar) shrink fit sleeves were utilized to produce a mechanical radial pressure of 30 to 195 MPa. Unconfined room temperature (RT) and HT experiments revealed that Ti2AlC fails in a gradual brittle (also referred to as graceful failure) manner with a low dependency on temperature up to 800°C. All experiments conducted with radial confinement produced a fully plastic response without failure. The addition of hydrostatic confinement increased the maximum compressive stress for all temperatures and allowed specimens to reach strains in excess of 8% without failing. Optical and Scanning Election Microscopy (SEM) images were taken of the cross-section of recovered confined specimens. Imaging revealed conical damage patterns on each end of the specimen which facilitate the plastic response.

ACKNOWLEDGMENTS

I would like to sincerely thank Dr. Arun Shukla for this opportunity to be a part of his lab and to undertake this work. If it had not been for the marvelous experiments of the DPML I would not have been inspired to pursue my master's degree. I am honored to work under such and intelligent, patient, and kind individual.

I would also like to thank my thesis committee members Hongyan Yuan and Richard Vaccaro for graciously accepting to help me on this endeavor. I would like to thank the Department of Mechanical, Industrial, and Systems faculty and staff for their assistance and instruction. Special thanks to Joe Gomez and Dave Ferreira for their many hours of help in the machine shop. I would like to thank Dr. Murat Yazici and Dr. Idris Karen for their assistance with my FEA modeling. I would like to thank Dr. Otto Gregory, Michael Platek, Dr. Carl-Ernst Rousseau, Akram Abbasi, and Everett Chrisman for offering their facilities, equipment and expertise for my SEM imaging.

I would like to thank my DPML colleagues: Nick Denardo, Mark Farat, Carlos Javier, Shyamal Kishore, Emad Makki, Helio Matos, Mike Pinto, Chris Salazar, Craig Tilton and Jefferson Wright who have helped me along the way with their friendship and input. I would especially like to thank Prathmesh Parrikar for his continuous guidance through training in experimental equipment and procedures to endless hours of discussion about experimental results.

I would like to thank the financial support provided by the Air Force Office of Scientific Research under Grant No. FA9550-13-1-0037 and the National Science Foundation under Gran No. CMMI 1233887.

I would like to thank: my parents for supporting me in every way possible throughout every aspect of life; my siblings for their continuous encouragement, and my wonderful wife for her steadfast love and patience; and finally the Lord for His abundant blessings and the ability to partake in this research.

TABLE OF CONTENTS

ABSTRACT ii

ACKNOWLEDGMENTS iii

TABLE OF CONTENTS v

LIST OF TABLES vii

LIST OF FIGURES viii

CHAPTER 1 1

INTRODUCTION 1

Background 1

Inspiration 2

Review of Literature 2

CHAPTER 2 5

THEORETICAL CONSIDERATIONS 5

Basic Theory 5

Specimen Geometry 6

Loading Conditions 7

Confinement Sleeve Design 9

High Temperature 13

CHAPTER 3 15

EXPERIMENTAL PROCEDURES 15

Material and Specimens 15

Experiments 16

Setup 17

Postmortem Evaluation 18

CHAPTER 4 20

RESULTS AND DISCUSSION 20

4.1 Unconfined Experiments 20

4.2 Confined Experiments 26

4.3 Discussion of Experiments 33

CHAPTER 5 36

SUMMARY 36

BIBLIOGRAPHY 37

LIST OF TABLES

Table 1: Confinement pressure (MPa) for experiments 16

Table 2: Material properties used to calculate confinement pressures 17

LIST OF FIGURES

Figure 1: Schematic of axisymmetric boundary value problem 10

Figure 2: Axisymmetric FEA models of assembly geometry where colors represent the percent of full confinement pressure calculated by lateral stress. (a) Low confinement sleeve unloaded confinement profile. (b) Low confinement sleeve at 2.0% strain. (c) Medium confinement sleeve unloaded confinement profile. (d) Medium confinement sleeve at 2.1% strain. (e) High confinement sleeve unloaded confinement profile. (f) High confinement sleeve at 2.9% strain. 12

Figure 3: Ti_2AlC specimens, from left to right: unconfined, low confinement, medium confinement, and high confinement. 16

Figure 4: Schematic of SHPB setup. 18

Figure 5: Typical pulse development for unconfined Ti_2AlC at a strain rate of 500 s^{-1}. 20

Figure 6: High speed camera images of unconfined Ti_2AlC specimen at RT tested on a SHPB at a strain rate of ~500 s^{-1}. (a) Undeformed specimen at 0 μs, (b) maximum stress reached at 36 μs, (c) first crack visible on the surface within the red loop at 46 μs, (d) cracks fully visible as the specimen continues to fail gradually at 59 μs, (e) complete separation of the two segments which are both being compressed by the bars creating stress reading on the plot at 78 μs, (f) true dynamic compressive stress-strain plot. 21

Figure 7: Force equilibrium of typical RT unconfined specimen represented by the compressive force on the front and back faces. 22

Figure 8: True compressive stress-strain plot of unconfined Ti_2AlC specimens at temperatures of 25 to 1000°C and strain rate of 500 s^{-1}. 23

Figure 9: Postmortem images of unconfined specimens tested at: (a) 25°, (b) 500°C, (c) 800°C and (d) 1000°C. 24

Figure 10: SEM images of fracture surfaces of unconfined specimens tested at: (a) 25°C, (b) 500°C, and (c) 800°C. 25

Figure 11: True compressive stress-strain response of confined Ti_2AlC at RT and a strain rate of 500 s^{-1} 26

Figure 12: True compressive stress-strain response of confined Ti_2AlC at confinement pressures of 30 to 135 MPa and temperatures of 500 to 1000°C at a strain rate of 500 s^{-1} 27

Figure 13: Optical microscope image of the sectioned ground and polished 500°C-75 MPa specimen. 29

Figure 14: Optical and SEM images of RT-75 MPa sectioned specimen. (a) Optical microscope image showing SEM image locations with an insert of entire sectioned specimen. (b) Cracked and highly damaged area making up cone boundary. (c) Area near the edge of the damage band. (d) Highly damage area inside of the damage band. (e) Area inside of the cones. (f) Area outside of the conical features 31

Figure 15: SEM images of the damage band of (a) RT-195 MPa specimen and (b) 1000°C-30±5 MPa specimen. 32

Figure 16: Average maximum stress vs. confining pressure plot of all tests..... 34

CHAPTER 1

INTRODUCTION

Background

MAX phases are layered ternary carbides and nitrides with hexagonal structure in the form $M_{n+1}AX_n$, where n varies from 1 to 3, "M" is an early transition metal, "A" is and A-group elements and "X" is C and/or N [1–4]. Most MAX phases have a unique combination of material attributes akin to both ceramics and metals. A few of their favorable properties likening them to ceramics are high elastic stiffness and service temperature along with low thermal expansion and low density [5–7]. They possess advantageous qualities associated with metals by being good electrical and thermal conductors as well as being relatively soft, easily machinable and damage tolerant [5, 7–9].

MAX phases are identified as kinking nonlinear elastic solids and are able to dissipate large amounts of energy by the formation of kink bands (KBs) when compressed due to their layered strong MX bonds and relatively weak MA bonds [1, 10]. At room temperature (RT) MAX phases normally fail in a brittle fashion however, they can reach a brittle to plastic transition (BPT) in HT [11, 12] and/or under sufficient hydrostatic confining pressure [10, 13].

Inspiration

Ti_2AlC is one particular phase that possesses all the aforementioned favorable characteristics. It has been a popular material to study because of its superior high temperature performance and low cost when compared to other MAX phases [2, 3]. With these extraordinary properties, Ti_2AlC has great potential for use in extreme thermal and mechanical loading environments such as hypersonic jets, structural applications, and protective armor. In order to use MAX phases to potentially develop safer and higher preforming, aircraft, structures and protection, their dynamic mechanical response must be better understood at high temperature and under confinement. The purpose of this study is to characterize the dynamic compressive response of Ti_2AlC when it is subject to high temperature loadings and under radial confinement.

Review of Literature

In the past 20 years interest in MAX phases has grown rapidly with Ti_2AlC getting considerable attention [1]. Many experiments have been performed on Ti_2AlC in various loading configurations and temperatures in these recent studies. Barsoum et al. measured the thermal and electrical properties, including thermal expansion, heat capacity and thermal conductivity, of Ti_2AlC in the temperature range of 25 to 1000°C [7]. A study by Radovic et al. has characterized the mechanical properties of polycrystalline Ti_2AlC from 300 to 1573 K using resonant ultrasound spectroscopy [6]. Also, the response of fully dense and 10 vol.% porous polycrystalline Ti_2AlC in uniaxial compressing at RT was analyzed by Zhou et al. and Poon et al. [9, 14].

Furthermore, Ti_2AlC's compressive performance at high temperatures, up to 900°C, was evaluated by Bai et al. [5]. At temperatures of 1150 and 1300°C, Barsoum et al. showed that Ti_2AlC's compressive response is completely plastic [8]. These studies only characterize the properties and quasi-static compressive response of Ti_2AlC.

Some dynamic experiments have been performed on Ti_2AlC using a Split Hopkinson Pressure Bar (SHPB) apparatus. RT dynamic experiments by Bhattacharya et al. were completed using a SHPB and 2-D high speed Digital Image Correlation (DIC) [15]. The strain rates varied from 500 to 4700 s^{-1} and a range of specimen L-D ratios from 0.2 to 0.8 were used. Abtula conducted high temperature dynamic experiments also using a SHPB [12]. These tests were completed at strain rates of 1500-4200 s^{-1} and temperatures ranging from RT to 1050°C. In addition, a study done by Naik Parrikar et al. evaluated the dynamic and quasi-static compressive constitutive behavior and fracture initiation toughness of fine grained Ti_2AlC [11]. The experiments were conducted using a modified SHPB apparatus with DIC and servo-hydraulic testing machine. The temperatures ranged from 25 to 1200°C while the strain rates coved 10^{-4} to 500 s^{-1}. Although many studies have been carried out on Ti_2AlC none have been completed with confinement.

In fact, only Guitton et al. and Bei, et al. have performed experiments on confined MAX phases to the authors knowledge [10, 13]. Guitton et al. performed RT and 900°C quasi-static tests (5×10^{-5} s^{-1}) on Ti_2AlN under an argon gas confinement pressure of 350 MPa. These specimens were parallelepipeds inserted in annealed aluminum cylinder assemblies to apply the gas compression. Bei et al. conducted

similar experiments on Ti_4AlN_3, TI_3AlC_2 and $Ti_3Al_{0.8}Sn_{0.2}C_2$ MAX phases except only at RT.

While dynamic confinement experiments have never been performed on MAX phases, many have been performed on ceramics. Of these studies the techniques of Chen and Ravichandran are of most interest. Chen and Ravichandran executed SHPB experiments on confined machinable glass ceramic (macor) and aluminum nitride (AlN) at RT [16–18]. Confinement was achieved via shirk fit sleeves of different materials for varying confined pressures of 10 to 230 MPa. Similarly, Nie completed SHPB confinement experiments on borosilicate glass, only he used a modified chamfered sleeve design and temperatures from RT to 600°C [19]. To date, dynamic experiments have not been performed on Ti_2AlC, or any MAX phase for that matter, with both high temperature and confinement. Therefore, this study seeks to explore the dynamic high temperature confined response of MAX phases, specifically Ti_2AlC.

CHAPTER 2

THEORETICAL CONSIDERATIONS

Basic Theory

The Split Hopkinson Pressure Bar (SHPB) is a testing apparatus that is used to measure the dynamic mechanical properties of materials. It operates at strain rates from 10^2 to 10^4 s^{-1}, which includes loading rates seen in car collisions and ballistic impacts [20]. The test consists of three bars, a striker, incident, and transmission bar, all of which are in the same axis. The specimen is placed between the incident and transmission bars. The striker bar impacts one end of the incident bar developing a one dimensional elastic strain wave. The compressive longitudinal wave propagates though the incident bar until it reaches the specimen. Upon which, some of the strain is transmitted through the specimen into the transmission bar while a portion is reflected back, creating a tensile strain wave in the incident bar. The strain in the bars is measured by strain gauges attached to the pressure bars, thus the specimen response can be captured using time resolved strain measurements. When equilibrium within the specimen is achieved, that is when Equation (1) is true, the stress, strain, and strain rate of the specimen are given by Equations (2), (3), and (4), respectively:

$$\varepsilon_i + \varepsilon_r = \varepsilon_t \tag{1}$$

$$\sigma_s = \frac{E_b A_b}{A_s}(\varepsilon_t) \tag{2}$$

$$\varepsilon_s(t) = \int_0^t \dot{\varepsilon}_s(t)dt \tag{3}$$

$$\dot{\varepsilon}_s = \frac{2C_b}{L_S}\varepsilon_r(t) \tag{4}$$

Where ε_i, ε_r, and ε_t are the incident, reflecting and transmitted strains measured by the strain gauges, σ_s is the stress in the specimen, E_b and A_b are the bar modulus and area, A_s is the specimen area, ε_s, and $\dot{\varepsilon}_s$ are specimen strain and strain rate, L_s is the length of the specimen, and C_b, is the longitudinal wave speed given by $\sqrt{E_b/\rho_b}$, where ρ_b is the bar density.

Specimen Geometry

The specimen length was chosen in order to measure an adequate reflected pulse amplitude for the desired strain rate. By rearranging Equation (4) the specimen length was calculated to be 8 mm using 500 s^{-1} for a strain rate and 400 με for the desired reflected strain. To ensure that the specimen would have enough time to reach equilibrium, the equilibrium time, t_e, in Equation (5), must be achieved before the critical strain, t_c in Equation (6), is reached.

$$t_e = n\frac{L_s}{C_s} \tag{5}$$

$$t_c = \frac{\varepsilon_c}{\dot{\varepsilon}_s} \tag{6}$$

Where n is the number of times the pulse is reflected within the specimen before equilibrium is achieved, L_s and C_s are the length and wave speed of the specimen, and ε_c is the critical strain of the specimen. It takes approximately four transits back and forth within a ceramic specimen before equilibrium is reached [21, 22]. Given the high stiffness and low density of Ti_2AlC it's wave speed of 8120 m/s is similar to ceramics.

Assuming it requires 4 transits to reach equilibrium t_e is just under 4 μs. Ti_2AlC is brittle and was expected to fail close to 1% strain, thus making t_c ~20 μs, suggesting that equilibrium will be easily attainable.

Traditionally, L/D ratios are kept near $\sqrt{3\nu_s/4}$, where ν_s is the Poisson's ratio of the specimen, to eliminated inertial effects [20, 23]. However, this would require a specimen diameter larger than the pressure bars themselves. It has been suggested that a ratio of 2:1 be used, similar to uniaxial compression testing for brittle materials, for high strain rate testing of high stiffness low failure strain specimens [22]. Because the specimen is stiff, small misalignment of the pressure bars can create stress concentrations that will lead to premature failure, which a shorter specimen would be more prone to. In addition, inertial effects are more significant for softer materials because the extra axial stress is on the order of 1 MPa for the strain rates develop by the SHPB [23]. Since inertia induced axial stress is a function of specimen material properties, radius, and strain acceleration, the stress can be further reduce by specimen geometry and loading conditions [23]. For these reasons, a diameter of 4.6 mm was chosen to achieve L/D ratio as close to 2:1 as practically possible for fabrication purposes. Acceleration can be minimized by having a constant strain rate, the method for achieving this will be discussed in the next section.

Loading Conditions

When testing stiff brittle materials on a SHPB many modifications must be made to accurately measure the material's response [24]. Brittle materials are more sensitive to stress dispersion caused by accelerations which can lead to premature failure. Since

the material is stiffer than the pressure bars and expected to fail at high stress when confined, special treatment of the bar contact faces is required. In addition, since the specimens will crack and fragment, the samples must only be loaded once for valid postmortem observations to be taken.

A constant strain rate loading minimizes stress dispersion and the time for the specimen to reach equilibrium. This condition can be created by using pulse shapers to modify the incident pulse. A pulse shaper is a small disk of plastically yielding material placed on the striker side of the incident bar to shape the stress wave profile. Because brittle materials are usually linearly elastic until failure a linear ramp profile is desirable, especially near failure point of the specimen. In this work copper pulse shapers were used and designed using the method outlined in reference [23].

Because the specimen is stiffer than the pressure bars the bar faces without alteration will indent during loading. This will cause stress concentrations in the specimen corners leading to premature failure. For this reason, tungsten carbide (CW) inserts were placed on each side of the specimen to keep the loading surface flat. The inserts were sized to match the impedance of the bars so that no pulse disturbance would occur. Inserts also protect the pressure bars from permeant deformation which could be caused by the high confinement specimens.

In order to make usable postmortem evaluations of the fragmented and/or damaged specimens it is important to only load the sample once. This was done using a moment trap which consisted of a screw on flange on impact end of the incident bar and a steel block acting as a rigid mass. A gap between the flange and the rigid mass was calculated using the incident pulse strain history in equation (7):

$$d = C_b \int_0^T \varepsilon_t(t)dt \tag{7}$$

Just after the incident pulse is transferred through the bar the flange contacts the rigid mass preventing the reflections within the incident bar from reloading the specimen.

Confinement Sleeve Design

A metal shrink fit sleeve was chosen to apply the desired radial confining pressure on the testing samples. The goal of the confining pressure is to produce a brittle to plastic transition of the MAX phase's dynamic compressive response. The pressure values were chosen based on other work where brittle materials reached or did not reach a ductile response [17, 18]. The confining pressure was approximated by solving an axisymmetric boundary value problem given by Equations (8) and (9) [16–18]. This equation assumes the specimen is an elastic solid cylinder, the sleeve is an elastic perfectly plastic hollow cylinder containing a plastic boundary. The equation also includes a misfit between the outer diameter of the specimen and the inner dimeter of the sleeve shown in Figure 1.

$$\frac{\delta}{2r_1} = (1+\nu_2)(1-2\nu_2)\left(\frac{\sigma_{\gamma_2}}{E_2}\right)\left[ln\left(\frac{r_1}{R}\right) + \frac{1}{2}\left(\frac{R}{r_2}\right)^2 - \frac{1}{2}\right] + (1-\nu_2{}^2)\left(\frac{\sigma_{\gamma_2}}{E_2}\right)\left(\frac{R}{r_1}\right)^2 + (1-\nu_1)\left(\frac{\sigma_{\gamma_2}}{E_1}\right)\left[ln\left(\frac{R}{r_1}\right) + \frac{1}{2}\left(1-\left(\frac{R}{r_2}\right)^2\right)\right] \tag{8}$$

$$P = \sigma_{\gamma_2}\left[ln\left(\frac{R}{r_1}\right) + \frac{1}{2}\left(1-\left(\frac{R}{r_2}\right)^2\right)\right] \tag{9}$$

Where δ is the interference between the specimen outer diameter and the sleeve inner diameter, E_1, ν_1, and r_1 are the specimen's elastic modulus, Poisson's ratio, and outer diameter, σ_{γ_2}, E_2, ν_2, and r_2 are the sleeve's yield stress, elastic modulus, Poisson's

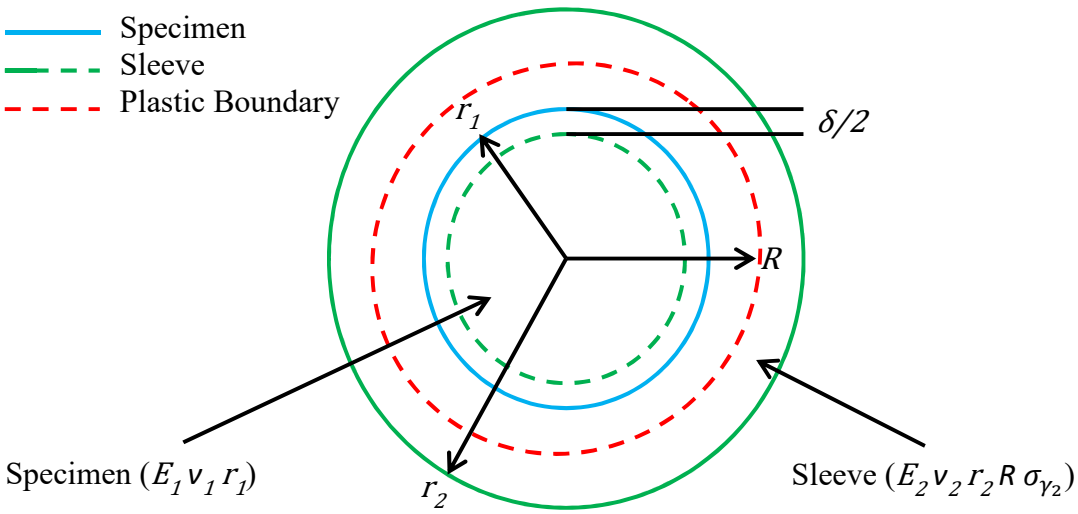

Figure 1: Schematic of axisymmetric boundary value problem

ratio, and outer diameter, R is the plastic boundary within the sleeve and P is the confining pressure exerted on the specimen by the sleeve. All values in Equation (8) are known except for the plastic boundary, R which can be solved. By inserting the found R value into Equation (9), the confining pressure, P can be retrieved. Because the sleeve is plastically yielding there is not a significant pressure change (~3%) if the misfit dimension is off by ±0.001 mm from the target 0.025 mm. This makes any inaccuracy in measurement low impact on the pressure keeping the confinement values consistent.

For the confinement sleeve, a chamfer design was chosen similar to what was used by X. Nie [19]. The benefits of this are twofold. First, it effectively prevents the sleeve from being loaded axially which can lead to inflated stress results and/or additional testing to artificially remove said load. Secondly, it preserves the confining pressure because the chamfers reduce the axial loading of the sleeve thus avoiding sleeve expansion due to Poisson's ratio. In previous work a separate test of the sleeve alone was used to approximate the stress in the sleeve in order to subtract the axial

contribution [16–18]. This not only takes extra materials and testing, but produces only an approximate sleeve contribution because the singular sleeve is in a different stress state than the assembled sleeve. When an unchamfered sleeve is loaded axially it expands due to poisons ratio thus relaxing the radial pressure. At a certain strain the confining pressure will be equal to zero as shown in Equation (10) [25]:

$$(\nu_2 - \nu_1)\varepsilon = \frac{\sigma_{\gamma_2}}{E_2} \tag{10}$$

With the selected materials the confining pressure would be zero at ~2% strain which is at or before the maximum stress of the confined specimens. To prevent the sleeve from relaxing a second chamfered sleeve has been used before [18]. Although, again the stress cannot be directly taken from the experimental results and the sleeve still experiences some relaxation.

Abaqus 6.14 was used to verify confinement pressure on the specimen. The MAX phase was modeled as elastic while the sleeve was modeled as elastic perfectly plastic. Modeling showed that the confining pressure exerted by the sleeve reduces near the ends of the specimen as shown in Figure 2a, 2c, and 2e. However, when the assembly is compressed the oblique sleeve-bar contact creates high radial pressure on the end faces, shown in Figure 2b, 2d, and 2f. This local elevated confinement pressure reduces damage due to stress concentrations at the specimen corners while allowing the majority of the specimen to sustain full confinement pressure.

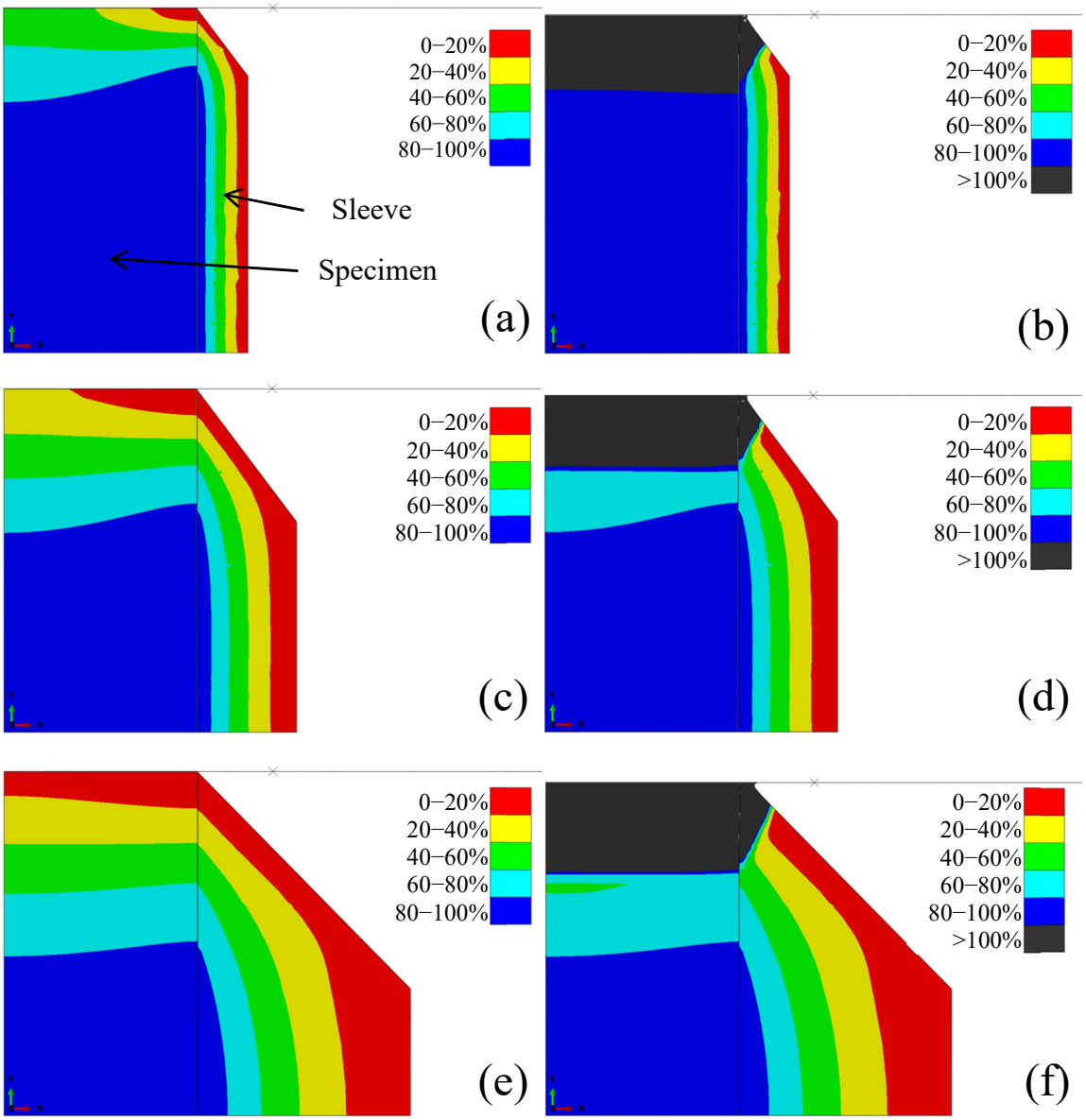

Figure 2: Axisymmetric FEA models of assembly geometry where colors represent the percent of full confinement pressure calculated by lateral stress. (a) Low confinement sleeve unloaded confinement profile. (b) Low confinement sleeve at 2.0% strain. (c) Medium confinement sleeve unloaded confinement profile. (d) Medium confinement sleeve at 2.1% strain. (e) High confinement sleeve unloaded confinement profile. (f) High confinement sleeve at 2.9% strain.

High Temperature

One concern high temperature poses is the thermal expansion of the sleeve, which reduces the interference mismatch resulting in loss of confining pressure. To combat the thermal growth Kovar, an iron-nickel-cobalt alloy manufactured by National Electronic Alloys, US, was chosen as the sleeve material. Kovar has a very low coefficient of thermal expansion for a large range of temperatures, thus it can sustain confining pressure at HTs. The thermal growth of the sleeves was calculated using the nominal coefficient of thermal expansion provided by the manufacture (National Electronic Alloys, US) through 900°C. For the 1000°C case the value was estimated by extrapolation. At high temperatures the material properties of both the specimen and the sleeve change. The modulus of the Ti_2AlC was provide by the manufacture (Kanthal®, Sweden) though 1400°C. The modulus and yield strength of Kovar was taken from the work of Zhou et al. [26] . However, his work does not provide values for temperatures as high as 1000°C. Thus, the modulus value was bounded with reasonable assurance between extrapolation of the existing data and the melting point of the material. The yield strength was measured in a high temperature compression test. The Poisson's ratio of both materials was assumed to be constant. Although Zhen showed a slight increase of Poisson's ratio for Ti_2AlC, changes of Poissons's for either material had very little effect on the confinement pressure calculation [27]. Because the temperature of the assembly would be measured from a thermocouple attached to the outer surface of the sleeve the temperature of the specimen could not be directly measured. To ensure that both the specimen and the sleeve were being heated evenly by induction heating, after assembly the temperature at the center of the specimen face

and at the outer surface of the sleeve were measured revealing no more than a 20°C difference for all the HT testing temperatures.

Another material property concern comes from the high heat required to assemble the confined specimens. During the assembly the shrink fit sleeve was exposed to ~1100°C to allow for the Ti_2AlC specimen to be inserted. Tensile tests were performed on the sleeve material to verify that the properties after heating were accurate for calculating confining pressure. The tests showed little to no degradation in modulus and yield strength.

An additional consideration has to do with the SHPB apparatus. When the thermal loading is applied to the specimen, heat also transfers to the pressure bars though conduction and radiation. A substantial rise in temperature of the bars will alter the properties, thus changing the wave speed and ultimately the experimental results. To prevent heating of the bars, water circulating copper coils were wrapped around the incident and transmission bars at the CW interface. The CW inserts also act as a thermal cushion preventing a sharp thermal gradient in the bars and increasing the length of the conduction path to the bars.

CHAPTER 3

EXPERIMENTAL PROCEDURES

Material and Specimens

Commercially available Ti_2AlC (Maxthal 211, Kanthal®, Sweden) was used for all experiments. The average particle size was 10μm with 80% of the grains falling between 1.5 and 23 μm. An extruded bar of Ti_2AlC was purchased and electrical discharged machined (EDM) into 5 mm diameter rods. The rods were then turned, parted and ground to 4.6 mm diameter 8 mm length cylinders. An image of the unconfined specimen is provided on the left in Figure 3.

Three different sleeves thicknesses of 0.58, 1.15, and 2.5 mm were fabricated out of Kovar. The interior holes were made by drilling and then boring with a tungsten carbide boring bar. The sleeves and specimens were matched so that the diameter misfit was 0.025±0.001 mm. Multiple measurements of the specimen outer dimeters and sleeve inner diameters were taken using a digital micrometer and small hole gage to ensure proper interference. Using an inducting coil, the sleeves were heated to approximately 1100°C so that the Ti_2AlC specimens could be inserted. Once the assembly cooled the end faces were ground and chamfered. The sleeved specimens are shown in Figure 3.

Figure 3: Ti_2AlC specimens, from left to right: unconfined, low confinement, medium confinement, and high confinement.

Experiments

All experiments were performed using a SHPB apparatus at a strain rate of approximately $500s^{-1}$. The tests were completed with temperatures varying from 25 to 1000°C and radial confinement pressures of 0 to 195 MPa. The temperature was supplied via an induction heater coil while the confinement was achieved by shrink fit confining sleeves. At least three successful experiments were completed for each of the 11 test environments shown in Table 1. The material properties used in the Equations (8) and (9) to create Table 1 are shown in Table 2. The subscripts 1 and 2 represent the specimen and sleeve material properties, respectively. The ±5 MPa for the 1000°C case is due to uncertainty of the sleeve modulus at that temperature. All RT values, thermal expansions and specimen modulus values were supplied by the manufacturers. The modulus and yield of the sleeve material was taken from reference [26]. Note that the interface mismatch, δ changes with temperature due to thermal expansion.

Table 1: Confinement pressure (MPa) for experiments

Temperature (°C)	Sleeve Thickness (mm)			
	None	0.58	1.15	2.50
25	0	75	135	195
500	0	-	75	135
800	0	-	-	75
1000	0	-	-	30±5

Table 2: Material properties used to calculate confinement pressures

T (°C)	E_1 (MPa)	E_2 (MPa)	ν_1	ν_2	σ_{y_2} (MPa)	δ (mm)	α_1 (10^{-6}/°C)	α_2 (10^{-6}/°C)
25	277	138	0.190	0.317	345	0.025	8.0	5.2
500	260	130	0.190	0.317	185	0.027	8.0	6.2
800	250	75	0.190	0.317	105	0.021	8.0	10.4
1000	240	35±10*	0.190	0.317	50†	0.015	8.0	12.6‡

*Extrapolated from reference [26]. †Calculated from compression test. ‡Extrapolated from manufacturer data.

Setup

The SHPB setup, shown in Figure 5, consisted of 12.7 mm diameter Maraging steel striker, incident and transmission bars. The nitrogen gas gun powered striker bar's length varied from 100 to 245 mm while the incident and transmission bars had lengths of 2133 and 1524 mm, respectively. A copper pulse shaper was placed on the impact of the incident bar. In addition, the end of the incident bar passed through a moment trap and was threaded to receive a screw on flange larger than the passage though the momentum trap. The specimens contacting faces were flanked by tungsten carbide (CW) inserts and lubricated by high vacuum grease. At the far end of the transmission bar was a rubber damper to halt the motion of the transmission bar. The strain gages attached to the incident and transmission bars were run through a 2310A signal conditioning amplifier in a half Wheatstone bridge configuration and connect to a Tektronix TDS3014C Digital Phosphor Oscilloscope for data collection. A Shimadzu HyperVision HPV-2 high speed video camera was used in conjunction with a Cordin Model 659 high energy flash lamp. The camera is capable of taking images at 1 million fps and was triggered by the oscilloscope.

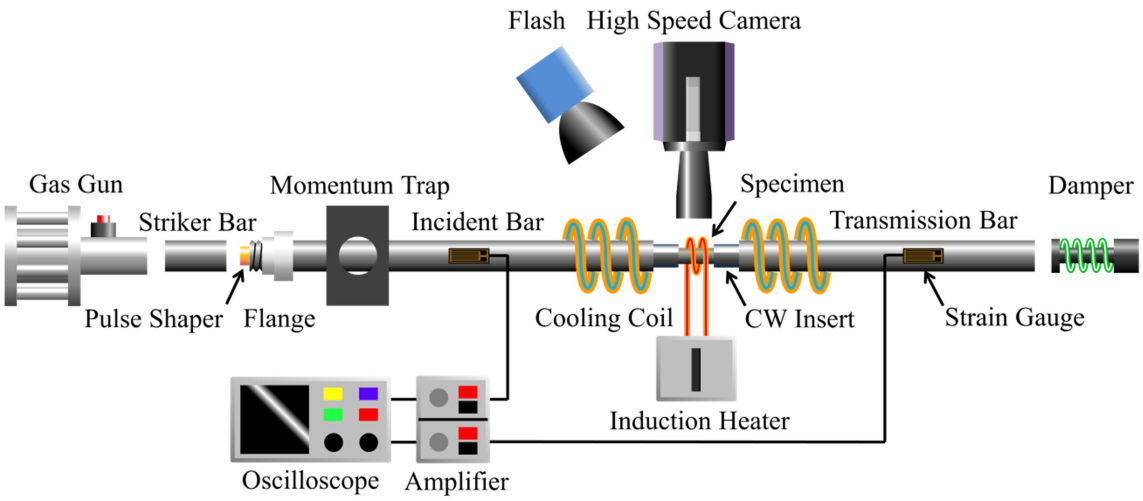

Figure 4: Schematic of SHPB setup.

For high temperature experiments, an Ajax Magnethermic Tocco induction coil heater was used to heat the specimens. In confined tests, a type k thermocouple was attached to the outer surface of the sleeve for temperature monitoring. Water circulating copper coils were looped around the incident and transmission bars near the heat source to cool the pressure bars. Boron nitride lubricant was used for high temperature tests instead of high vacuum grease.

Postmortem Evaluation

The remains of each of the unconfined experiments were observed using a Nikon SMZ-U stereoscopic microscope. The fracture surfaces were also observed using a Zeiss SIGMA VP Field Emission-Scanning Electron Microscope (FE-SEM). Because TI_2AlC is conducive the specimens did not required any preparation.

A select few of the confined experiments were also observed using the FE-SEM. The assemblies were sections using a Buehler IsoMetTM 1000 Precision Sectioning Saw with a diamond blade. The sections were then mounted in an epoxy resin and

ground and polished using a Buehler MetaServ 250 Grinder-Polisher. SiC paper was used starting with 240grit and ending with 600grit. Then 9, 3 and 1 μm diamond suspension was used finishing with 0.05 micron alumina polishing suspension. The specimens were etched in a $HF:HNO_3:H_2O$=1:1:2 for 15 seconds.

CHAPTER 4

RESULTS AND DISCUSSION

4.1 Unconfined Experiments

Typical incident, transmitted, and reflected pulses recorded by the oscilloscope are shown in Figure 5. The incident pulses developed had a nearly linear incline and a magnitude greater than the peak of the transmitted pulse while the reflected pulses achieved high magnitudes before the specimen reached its maximum stress. Wedge shaped transmitted pulses were developed through the unconfined specimens.

For the RT unconfined experiments, a high speed camera was used to capture the deformation process. The high speed camera images and the true stress-strain response of unconfined Ti_2AlC at 25°C experiment are shown in Figure 6. As seen in the Figure 6a-d, macroscopic cracks are not apparent on the surface until well after the maximum stress has been reached.

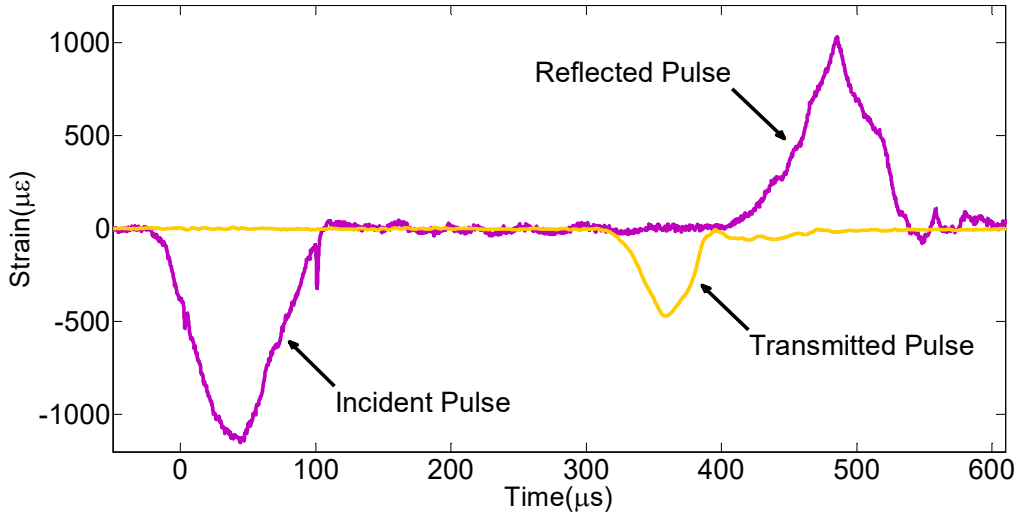

Figure 5: Typical pulse development for unconfined Ti_2AlC at a strain rate of 500 s^{-1}.

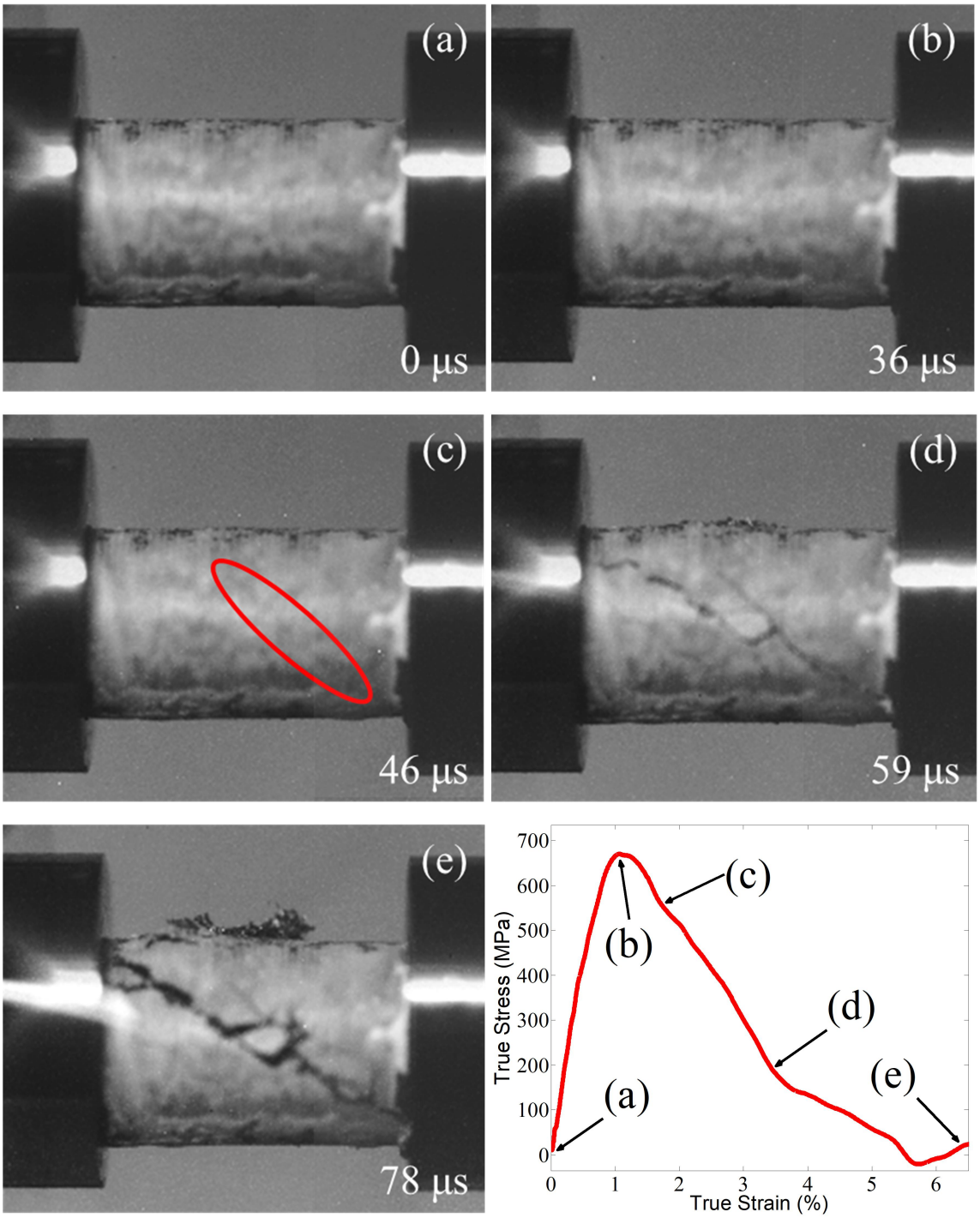

Figure 6: High speed camera images of unconfined Ti_2AlC specimen at RT tested on a SHPB at a strain rate of ~500 s^{-1}. (a) Undeformed specimen at 0 µs, (b) maximum stress reached at 36 µs, (c) first crack visible on the surface within the red loop at 46 µs, (d) cracks fully visible as the specimen continues to fail gradually at 59 µs, (e) complete separation of the two segments which are both being compressed by the bars creating stress reading on the plot at 78 µs, (f) true dynamic compressive stress-strain plot.

Depicted in Figure 6e, the specimen has one major fracture plane splitting it into two sections. This failure behavior was not uncommon for the RT specimens. Figure 6f displays typical RT dynamic compressive behavior of Ti_2AlC. The rising portion of the stress-strain curves for all the RT plots is nearly linear with the declining portion displaying the characteristic gradual nature, sometimes referred to as graceful, failure of Ti2AlC [1, 7]. In this experiment, force equilibrium was maintained until just after 5% strain. In general, force equilibrium was maintained throughout nearly the whole experiment. In Figure 7 a typical force equilibrium plot is shown. Note that there are small deviations in equilibrium, initially, when the camera and flash are triggered by the incident pulse, and when the specimen response relaxes resulting in a slope change.

For the HT unconfined experiments temperatures of 500, 800, and 1000°C were applied to the specimens. The constitutive behavior seen for the HT unconfined specimens is shown in Figure 8. All samples form wedge shaped plots with the rising portion being steeper than the unloading portion. The initial slopes appear to be the

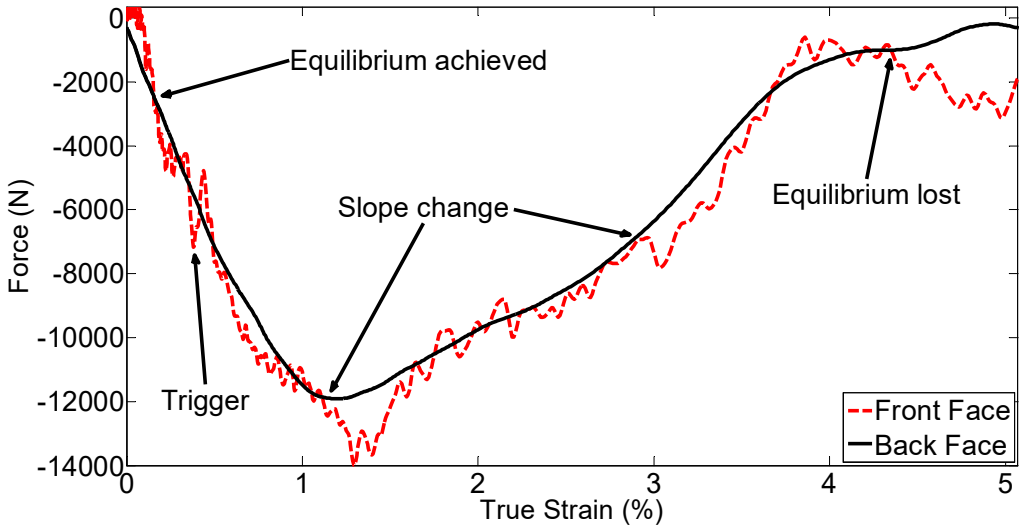

Figure 7: Force equilibrium of typical RT unconfined specimen represented by the compressive force on the front and back faces.

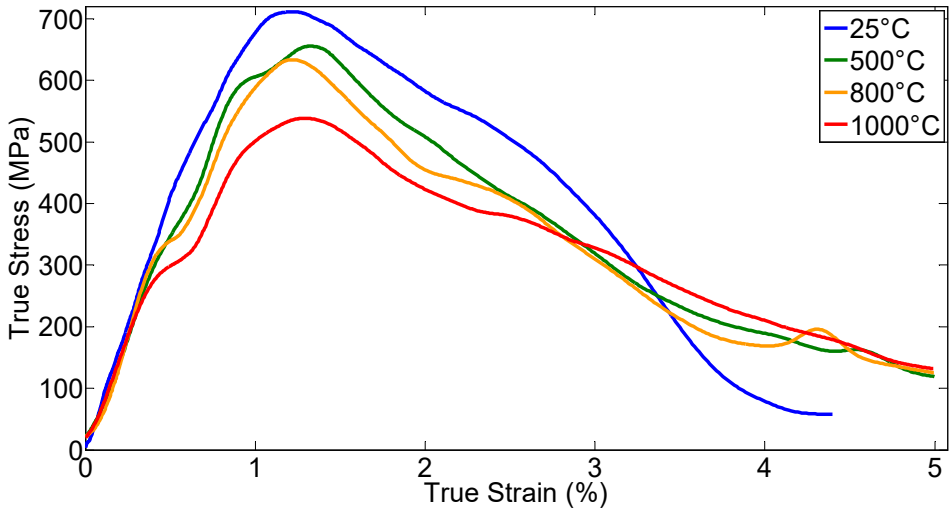

Figure 8: True compressive stress-strain plot of unconfined Ti_2AlC specimens at temperatures of 25 to 1000°C and strain rate of 500 s^{-1}.

same for all temperatures although for the very beginning of the plots force equilibrium is not fully achieved. It appears that the second half of the raising slope becomes less steep with increase in temperature. The maximum stress decreases with increasing temperature. On average the RT unconfined specimens reached a maximum stress of 704 MPa. From 25 to 800°C the maximum stress drops by just over 12% while from 25 to 1000°C, it drops by around 25%. At 25°C the maximum stress occurred at just below 1.2% strain on average while at 1000°C it was reached at over 1.4% strain on average. The failure response after the maximum stress becomes more gradual with the increase in temperature. Because the heating coil obstructs the view of the specimen, during the unconfined HT test, high speed imaging was not possible.

Postmortem images were taken of the specimens using an optical and scanning electron microscope (SEM). Shown in Figure 9 are the optical images of the unconfined specimens. All specimens tested at 25 to 800°C exhibited fragmentation into two to four major pieces.

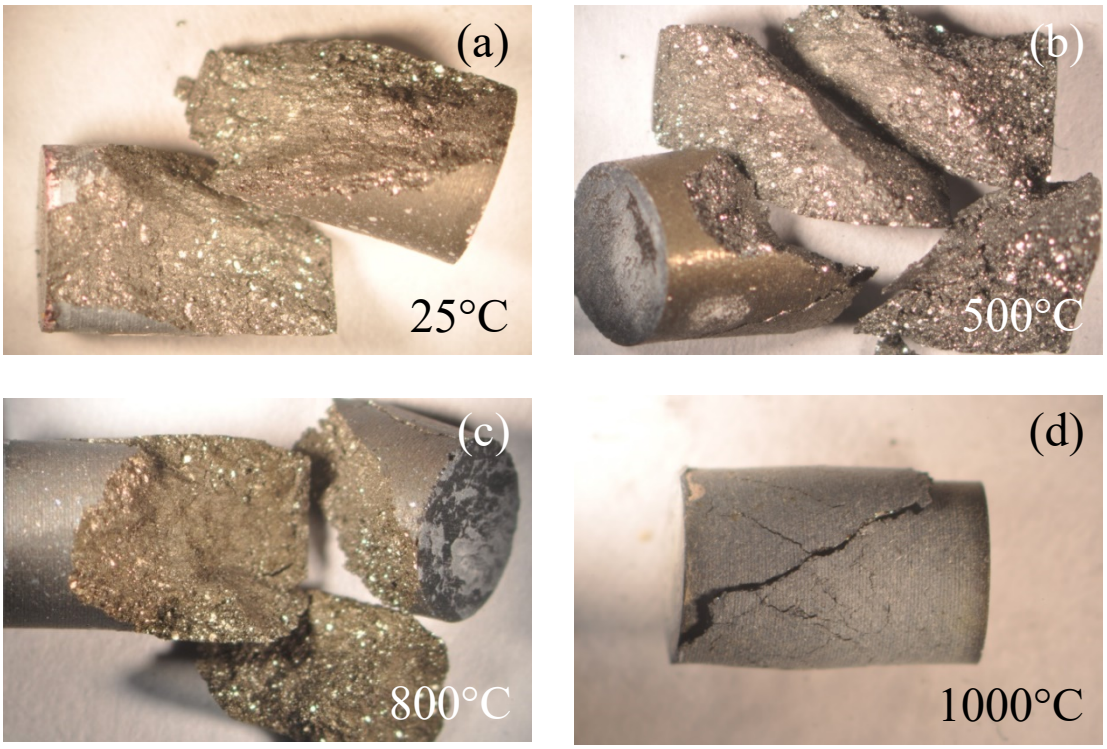

Figure 9: Postmortem images of unconfined specimens tested at: (a) 25°, (b) 500°C, (c) 800°C and (d) 1000°C.

When specimens separated into two sections the fracture plane split them in nearly equal halves. The 1000°C experiments did not split apart but showed similar major fracture planes. The angle of the fracture surface relative to the loading axis was measured to be approximately 30° for all testing temperatures

In Figure 10, SEM images of the 25, 500, and 800°C experiments are shown. At all these temperatures the micrographs revealed kink bands (KB), delaminations and intergranular and transgranular cracks. The density of KBs increased for the 500 and 800°C specimens while the frequency of cracking decreased. This is clearly seen when comparing Figure 10a to 10b. In Figure 10a, one defined kinked grain and many cracks are visible including a large mixed mode facture opposed to the extensive matrix of KBs in Figure 10b.

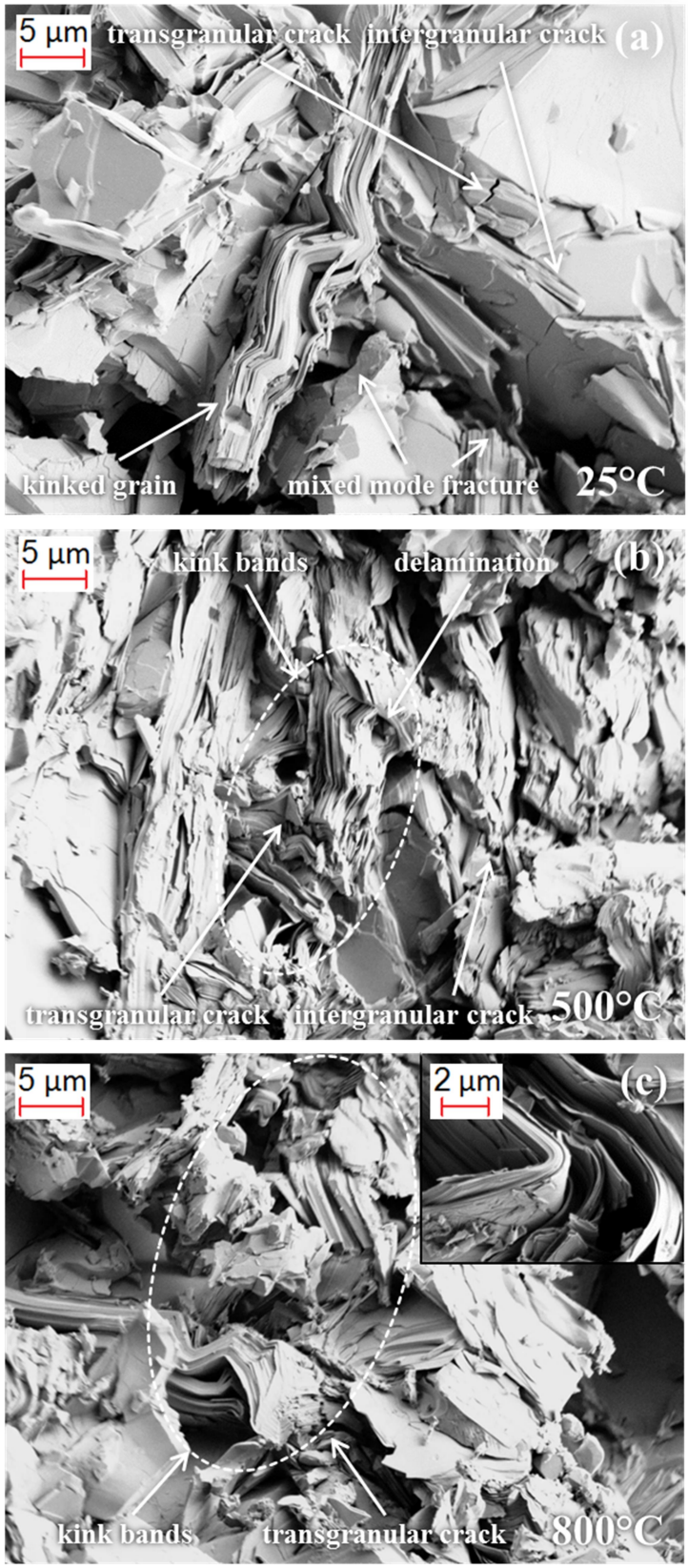

Figure 10: SEM images of fracture surfaces of unconfined specimens tested at: (a) 25°C, (b) 500°C, and (c) 800°C.

The extent of delamination observed also increased with temperature as depicted in the insert of Figure 10c which shows a highly angled and delaminated kinking band.

4.2 Confined Experiments

A low, medium, and high confinement sleeve designs were used to create confining pressures of 75, 135, and 195 MPa, respectively at RT by varying the wall thickness of the sleeves. The loading pulses for the confined experiments were very similar to those shown in Figure 5 only the incident pulse amplitudes were greater. Figure 11 shows the RT compressive stress-strain response of the confined specimens at a strain rate of 500 s^{-1}. The unconfined RT plot is included for reference and plots are shifted along the x-axis to make their features more observable. All the confinement sleeves yielded a brittle to plastic transition. It is clearly seen that after the maximum stress, the confined specimens maintain strength and plastically deform until the load is relieved. These tests stopped arbitrarily at the end of loading pulse and the specimens did not fail even after some reached strains greater than 9%. The

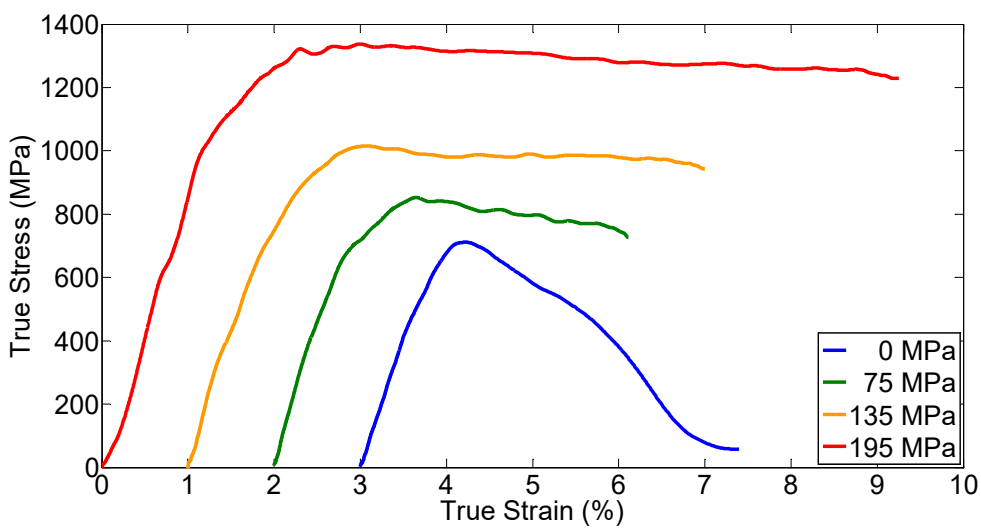

Figure 11: True compressive stress-strain response of confined Ti_2AlC at RT and a strain rate of 500 s^{-1}.

initial slopes appear to be the same for all experiments. However, the slope of the plastic region flattens with increasing confinement pressure. The low, medium, and high confinement sleeves exerted pressures on the specimen equal to approximately 10, 20, and 30% of the dynamic compressive strength of the unconfined specimen, respectively. They in turn increased the maximum compressive strength by approximately 20, 45, and 85%, respectively while changing the response from brittle failure to a fully plastic response.

HT experiments were performed on the confined specimens at temperatures of 500, 800, and 1000°C. As a result of the temperature, the confining pressures decreased: at 500°C the medium and high confinement sleeves applied pressures of 75 and 135 MPa, respectively; at 800 and 1000°C the high confinement sleeve produced a pressure of 75 and 30±5 MPa, respectively. Figure 12 shows the typical confined HT experiment results. Again, all confined tests produced a plastic response which reached an arbitrary strain where the experiments ended. As seen in all of the

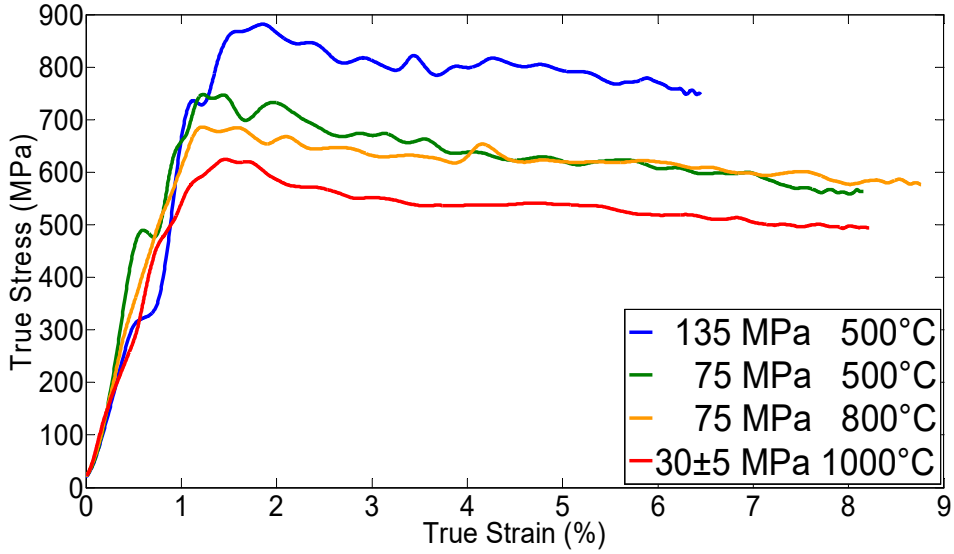

Figure 12: True compressive stress-strain response of confined Ti_2AlC at confinement pressures of 30 to 135 MPa and temperatures of 500 to 1000°C at a strain rate of 500 s^{-1}.

experiments, the confined HT test display a common initial slope. As seen in the HT unconfined experiments, increase in temperature lowers the maximum stress and reduces the slope of the post maximum stress region. With a confinement pressure of 135 MPa at 500°C a maximum compressive strength of 862 MPa on average was achieved, which is greater than the unconfined RT maximum stress. Furthermore, at 75 MPa confining pressure and 800°C, the maximum stress reached was equal to the unconfined RT specimens. In addition, a maximum stress of 616 MPa was attained at 1000°C with a confining pressure of 30±5 MPa opposed to only 532 MPa without confinement at that temperature.

No damage was visible on the impact faces of the recovered specimens. Four specimens were sectioned, ground and polished for microscope imaging. The 500°C-75 MPa sectioned specimen is shown in Figure 13. All sectioned specimens reveal symmetrical damage patterns within the specimen similar to the findings of Chen et al. [17, 18]. Conical features on each end of the specimen formed an hourglass shape. Within the hourglass cones the surface appears smooth with very few pores while outside the surface is very rough with many cavities. The conical boundaries between the two regions consist of bands of cracks and highly damage grain structure. Major crack separation was also seen along the interface in some specimens. Observation of the highest RT confinement and highest temperature tests shows little to no gaps along the cone boundary. The cracks along the damage band are believed to initially propagate due to high stress concentration at the specimen's corners [17]. Notice that some cracks do not originate at the extreme corners of the specimen but instead well inside of the sleeve.

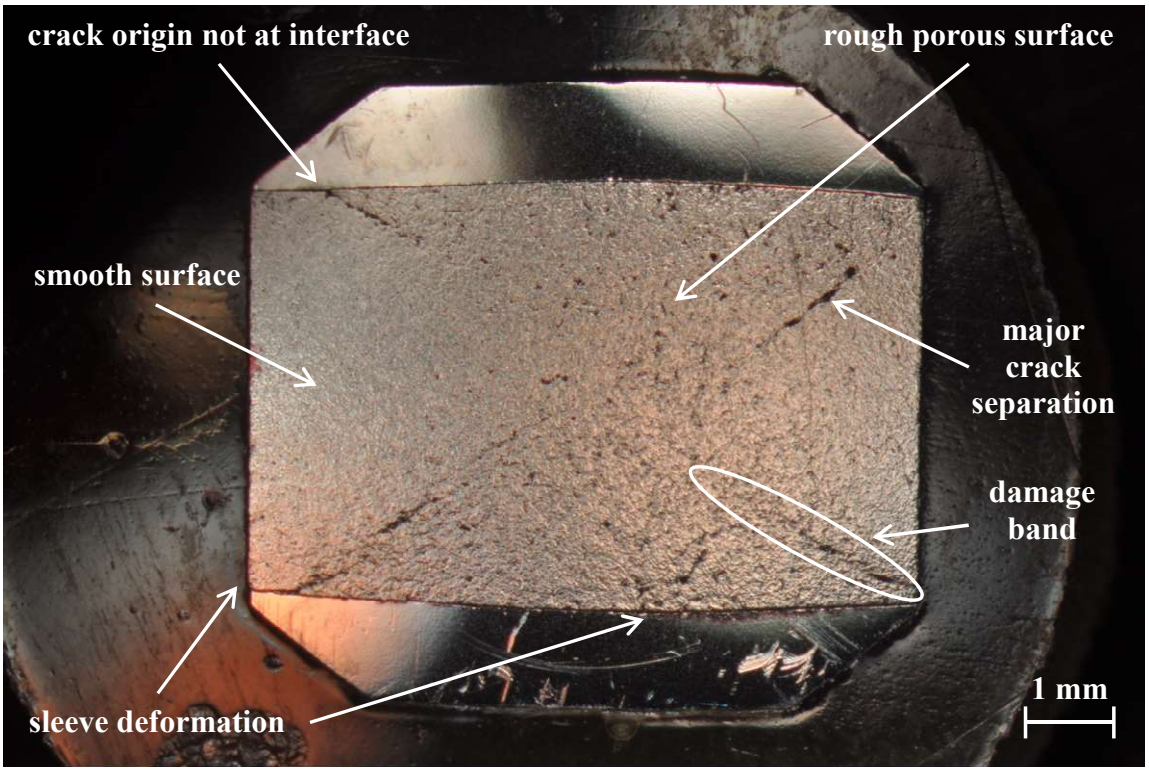

Figure 13: Optical microscope image of the sectioned ground and polished 500°C-75 MPa specimen.

It is supposed that the elevated confinement pressure at the end faces of the specimen, shown in Figure 2, could have prevented the crack from forming at the highly stress concentrated corner. The cracks are then only able to exist in lower pressure regions further away from the impact faces. Local damage at the corners of the sleeve was observed due to plastic deformation by either flatting and/or bending inward. At elevated temperatures the bowing of the sleeve interface near the middle of the specimen was much more evident than in RT sectioned images. This would appear to be due to the reduced yield strength of the sleeve at HTs. The cone apex angle for the 25°C and 500°C-75 MPa sectioned specimens remained at approximately 60 degrees forming a similar angle to the unconfined specimen's fracture plane. However, the cone angles for the 25°C-195 MPa and 1000°C-30±5 MPa were much greater being approximately 100 and 85 degrees, respectively.

SEM images were also taken of the confined sections. In initial images grain boundaries were hard to make out and no cracks or cavities were apparent in the structure except for those already visible optically. To make the boundaries clearer the specimens were etched. Etching removed $TiAl_x$ intermetallic from between the grains structures leaving some absences. SEM images for the RT-75 MPa specimen are shown in Figure 14. In Figure 14a the location of the SEM images are marked on an optical microscope image. The insert shows the entire sectioned specimen for reference. Figure 14b shows the damage band within the loop discernible by many cavities and cracks extending towards the center of the specimen. Also observable within the damage band is grain gliding on long grains parallel with the band. The damage bands do not maintain a constant width or reach the center of the specimen. All portions within the specimen exhibit intragranular cracking. Figure 14c shows a region on the edge of the damage band where cracks formed at the conical interface and minimal cavities were formed. Intergranular and transgranual cracks are easily visible along with voids left from the etching. Few grains are damaged showing minor delaminations dispersed throughout and misshapen boundaries. In Figure 14d the state of the highly deformed grains within the band which form the hourglass contour are shown. This region is not only riddled with cracks but many large cavities have developed. The majority of the grains are damaged and KBs in larger grains are present. These features suggest large relative motions took place on each side of the cone creating high strains in these grains. The area within the hourglass is shown in Figure 14e. This compacted region reveals almost no cavities and very small gaps between grains which explain the smooth surface finish in the optical images.

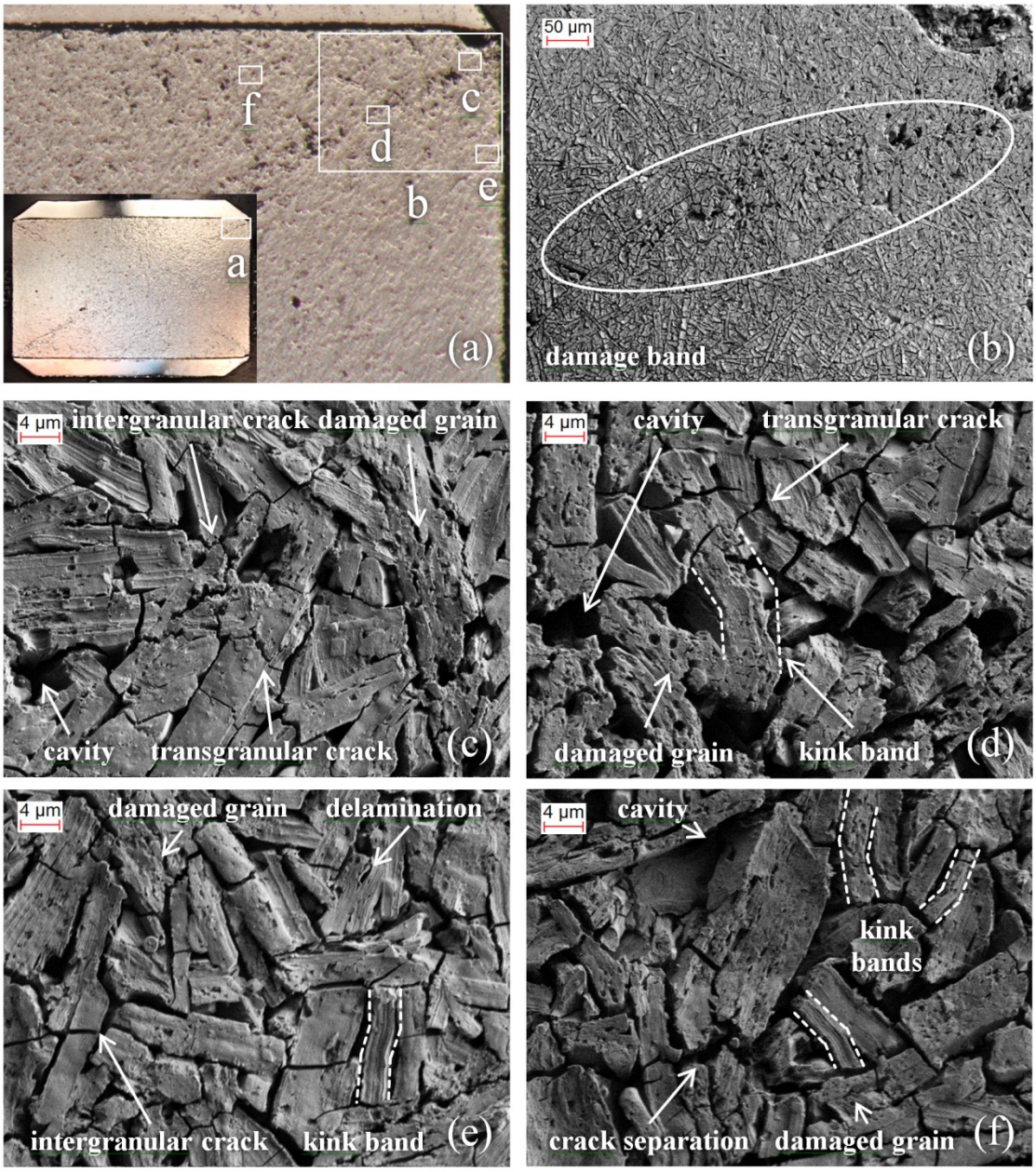

Figure 14: Optical and SEM images of RT-75 MPa sectioned specimen. (a) Optical microscope image showing SEM image locations with an insert of entire sectioned specimen. (b) Cracked and highly damaged area making up cone boundary. (c) Area near the edge of the damage band. (d) Highly damage area inside of the damage band. (e) Area inside of the cones. (f) Area outside of the conical features

The grain structure shows marginal damage with some delamination and very few kinked grains. From the images it is apparent that the area inside of the cones was highly compressed on all sides. Figure 14f shows a portion outside of the cones. In this image many of the grains are damaged and multiple KBs are seen in smaller

grains. Cavities are present and the intergranular cracks have separated leaving larger spaces between grain structures which are largely responsible for the rough surface appearance of the expansion section. Due to the features observed it is clear that this section expands radially during axial compression of the specimen.

In Figure 15, SEM images of the damage band of the RT-195 MPa and 1000°C-30±5 MPa specimens are shown. Unlike the RT-75 MPa test, both of these highly damage regions along the cone boundary contain very few cavities despite both reaching double the strain value. Within the damage band of the 1000°C-30±5 MPa shown in Figure 15b extensive delamination is seen compared to that of the two RT confined test images (Figure 14d and 15a). In addition, the grain structures contain significantly less transgranular cracks and are so mangled and distorted it is hard to tell where many of the boundary's lie. These results mimic the damage mechanisms seen in the unconfined tests where KB density and delamination increased with temperature and the prevalence of cracks diminished.

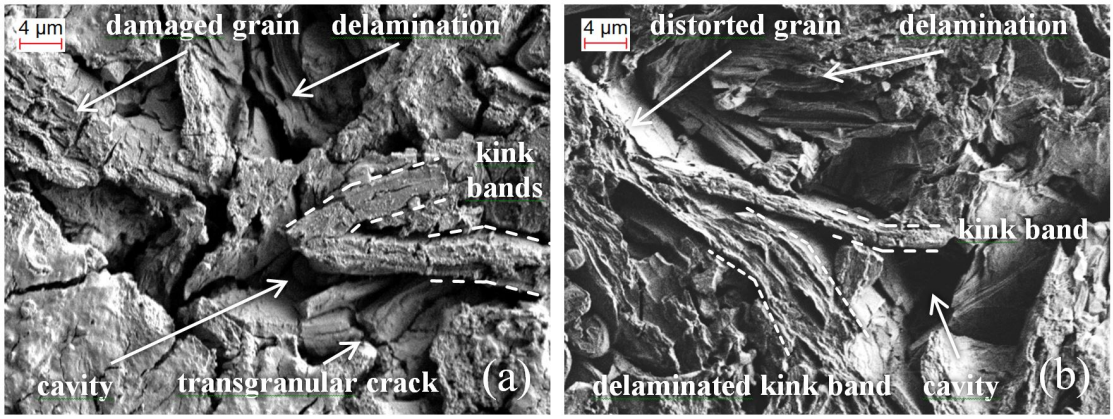

Figure 15: SEM images of the damage band of (a) RT-195 MPa specimen and (b) 1000°C-30±5 MPa specimen.

4.3 Discussion of Experiments

MAX phase Ti_2AlC specimens under unconfined conditions soften as the temperature is increased inhibiting brittle crack propagation. Thus, weakening the material and increasing the formation of KBs and delamination. Since the development of KBs and delaminations requires high strain and is energy intensive, the apparent higher frequency of KBs and delaminations at HTs is likely responsible for the increasingly gradual failure observed.

In the confined experiments, the radial pressure applied by the confinement sleeves increased the stress required for cracks to propagate within the specimen thereby increasing the strength of the specimen. Likewise, the restriction of crack propagation induced a plastic response in the regularly brittle MAX phase. From observation of the specimens, it is apparent that the two cones making up the hourglass profile move inward when compressed. This motion is accommodated by the deformation and gliding of grains along the conical interface in addition to cracking and radial expansion of the material outside of the hourglass against the sleeve. Based on the work of Chen W. et al. [17, 18], the cracks along the cone boundary begin to propagate and accumulate damage primarily after the maximum stress is reached. According to Bei et al. [10], the localized damage in the bands is the reason for the plastic response. As observed in the SEM micrographs, at low temperatures the main damage mechanisms are cracking and kinking. Specimens with lower confining pressures and temperature subjected to higher strains showed major crack separation along the conical boundaries. At elevated temperatures, fewer cracks were present and delamination was prominent. The radial confinement prevents the

specimen from separating and creates additional friction along the crack surfaces. This friction impedes the growth of sliding cracks thus producing a fully plastic response.

The average maximum stress achieved for each test condition is plotted in Figure 16. As displayed by the unconfined experiments, an increase in temperature causes slight decrease of roughly 12% in strength through 800°C. After which, at 1000°C the maximum failure stress declines significantly by about 25%. These results agree with increased deterioration of Ti_2AlC which has been observed at over 800-900°C [5, 11, 12]. All the unconfined specimens failed in a brittle fashion with a progressively gradual post maximum stress response with increasing temperature.

Remarkably, the response of all confined tests was plastic allowing the material to reach strains in excess of 9% without failure. As expected, the addition of a confinement sleeve boosted the maximum stress with increase of confining pressure. For the confined RT experiments the improvement in load bearing of the specimen seems to escalate with higher confinement. The maximum stress increased by 20% with just over 10% of the unconfined failure stress applied as confinement pressure.

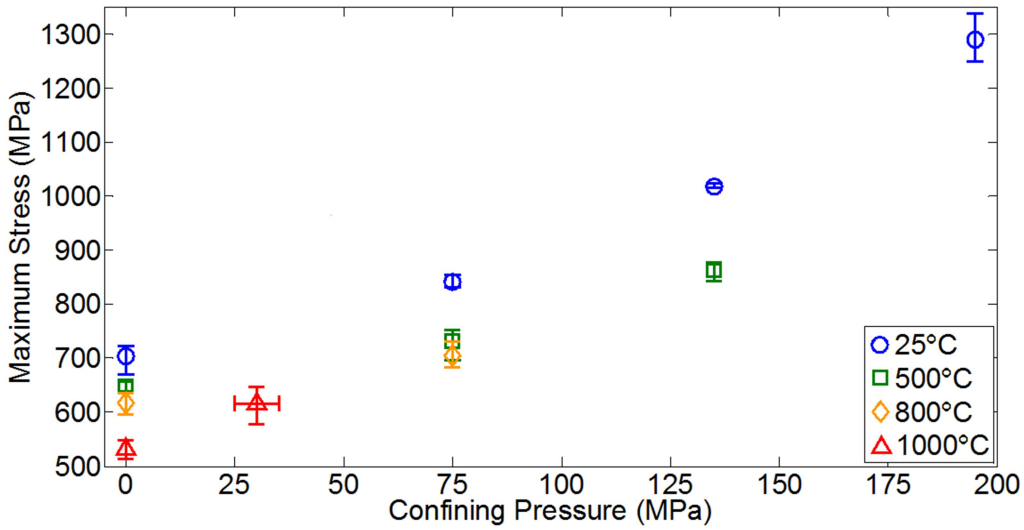

Figure 16: Average maximum stress vs. confining pressure plot of all tests.

While an increase of almost 85% in maximum stress was observed when 30% of unconfined failure stress was applied for confinement. This same trend is present for the 500°C experiments, where increase in maximum stress improves slightly with increasing confinement pressure. It is interesting to note that at 800°C a confinement pressure of 75 MPa increased the maximum strength more than at 500°C. Furthermore, the 1000°C-30±5 MPa experiments show very high increase in compressive strength given that only 30±5 MPa was applied in confining pressure. Thus, from these experiments it can be conjectured that at low confinement the effectiveness of the hydrostatic pressure increases with increase in temperature.

CHAPTER 5

SUMMARY

Experiments were performed to evaluate the dynamic mechanical response of Ti_2AlC at HT and under radial confinement. The dynamic experiments were conducted in thermal environments ranging from 25 to 1000°C and under radial pressures of 30 to 195 MPa. Unconfined RT and HT experiments revealed that Ti_2AlC fails in a gradual brittle manner with a low dependency on temperature up to 800°C. At 1000°C the unconfined Ti_2AlC only showed a 25% reduction in maximum failure stress. All experiments conducted with radial confinement produced a fully plastic response without failure. Strains in excess of 8% were achieved in confined tests for all testing temperatures. Increase in confining pressure result in increase in strength of the MAX phase. A confinement pressure of 195 MPa at RT produced an increase in maximum compressive strength of nearly 585 MPa. At 1000°C a confinement pressure 30±5 MPa increases the compressive strength by 85 MPa. Confined specimens contained conical damage patterns at each end with the apexes near the center. These features forming an hourglass shape contained cracks and damaged grain structure which facilitates the plastic response of the confined specimens. In both the confined and unconfined experiments, increase in temperature increased the density of KBs and delaminations while the prevalence of transgranular and intergranular cracking diminished.

BIBLIOGRAPHY

1. Barsoum MW (2013) MAX Phases: Properties of Machinable Ternary Carbides and Nitrides. Wiley-VCH Verlag GmbH & Co. KGaA, Weinheim, Germany
2. Zhou A (2008) Kinking Nonlinear Elastic Solids: Theory and Experiments. Drexel University
3. Barsoum MW, Radovic M (2011) Elastic and Mechanical Properties of the MAX Phases. Annu Rev Mater Res 41:195–227. doi: 10.1146/annurev-matsci-062910-100448
4. Radovic BM, Barsoum MW (2013) MAX phases : Bridging. Am Ceram Soc Bull 92:20–27.
5. Bai Y, He X, Wang R, et al (2013) High temperature physical and mechanical properties of large-scale Ti2AlC bulk synthesized by self-propagating high temperature combustion synthesis with pseudo hot isostatic pressing. J Eur Ceram Soc 33:2435–2445. doi: 10.1016/j.jeurceramsoc.2013.04.014
6. Radovic M, Barsoum MW, Ganguly a., et al (2006) On the elastic properties and mechanical damping of Ti3SiC2, Ti3GeC2, Ti3Si0.5Al0.5C2 and Ti2AlC in the 300-1573 K temperature range. Acta Mater 54:2757–2767. doi: 10.1016/j.actamat.2006.02.019
7. Barsoum MW, Salama I, El-Raghy T, et al (2002) Thermal and electrical properties of Nb2AlC, (Ti, Nb)2AlC and Ti2AlC. Metall Mater Trans A 33:2775–2779. doi: 10.1007/s11661-002-0262-7
8. Barsoum MW, Brodkin D, El-Raghy T (1997) Layer Machinable Ceramics for

High Temperature Applications. Scr Mater 36:535–541.

9. Poon B, Ponson L, Zhao J, Ravichandran G (2011) Damage accumulation and hysteretic behavior of MAX phase materials. J Mech Phys Solids 59:2238–2257. doi: 10.1016/j.jmps.2011.03.012

10. Bei G-P, Guitton A, Joulain A, et al (2013) Pressure-enforced plasticity in MAX phases: from single grain to polycrystal investigation. Philos Mag 93:1784–1801. doi: 10.1080/14786435.2012.755272

11. Naik Parrikar P, Benitez R, Gao H, et al (2016) Mechanical response of fine grained Ti2AlC under extreme thermo-mechanical loading conditions. Mater Sci Eng A 658:176–184. doi: 10.1016/j.msea.2016.01.106

12. Abotula Sandeep (2013) Dynamic Response of Aerospace Materials under Extreme Environ. University of Rhode Island

13. Guitton A, Joulain A, Thilly L, Tromas C (2014) Evidence of dislocation cross-slip in MAX phase deformed at high temperature. Sci Rep 4:6358. doi: 10.1038/srep06358

14. Zhou AG, Barsoum MW, Basu S, et al (2006) Incipient and regular kink bands in fully dense and 10 vol.% porous Ti 2AlC. Acta Mater 54:1631–1639. doi: 10.1016/j.actamat.2005.11.035

15. Bhattacharya R, Benitez R, Radovic M, Goulbourne NC (2014) High strain-rate response and deformation mechanisms in polycrystalline Ti2AlC. Mater Sci Eng A 598:319–326. doi: 10.1016/j.msea.2014.01.032

16. Chen W, Ravichandran G (1994) Dynamic compressive behaviour of ceramics under lateral confinement. Le J Phys IV 4:C8-177-C8-182. doi:

10.1051/jp4:1994825

17. Chen W, Ravichandran G (1996) Static and dynamic compressive behavior of aluminum nitride under moderate confinement. J Am Ceram Soc 79:579–584.

18. Chen W, Ravichandran G (1997) Dynamic Failure of a Glass Ceramic. J Mech Phys Solids 45:1303–1328.

19. Nie X (2010) Dynamic Failure of Borosilicate Glass Under Various Loading Conditions. Purdue University

20. Shukla A, Dally JW (2014) Experimental Solid Mechanics, 2nd ed. College House Engerprises, LLC, Knoxville, Tennessee

21. Ravichandran G, Subhash G (1994) Critical Appraisal of Limiting Strain Rates for Compression Testing of Ceramics in a Split Hopkinson Pressure Bar. J Am Ceram Soc 77:263–267. doi: 10.1111/j.1151-2916.1994.tb06987.x

22. Subash G, Ravichandran G (2000) Split-Hopkinson Pressure Bar Testing of Ceramics. 8:497–504. doi: 10.1361/asmhba0003299

23. Chen W, Song B (2011) Split Hopkinson (Kolsky) Bar: Design, Testing and Applications. Eff Br mindfulness Interv acute pain Exp An Exam Individ Differ. doi: 10.1017/CBO9781107415324.004

24. Frew DJ, Forrestal MJ, Chen WW (2002) Pulse shaping techniques for testing brittle materials with a split Hopkinson pressure bar. Exp Mech 42:93–106. doi: 10.1177/0018512002042001794

25. Chen W (1995) DYNAMIC FAILURE BEHAVIOR OF CERAMICS. California Institute of Technology

26. Zhou Y, Bao FH, Ren JL, North, T H (1991) Interlayer selection and thermal

stresses in brazed si3N4-steel joint. Mater Sci Technol 7:863–868.

27. Zhen T (2004) Compressive Behavior of Kinking Nonlinear Elastic Solids - Ti3SiC2, Graphite, Mica and BN. Drexel University